UCSF
UC San Francisco Previously Published Works

Title

Dynamic diffusion-weighted hyperpolarized 13C imaging based on a slice-selective double spin echo sequence for measurements of cellular transport

Permalink

https://escholarship.org/uc/item/9pn322gj

Journal

Magnetic Resonance in Medicine, 81(3)

ISSN

0740-3194

Authors

Zhu, Xucheng
Gordon, Jeremy W
Bok, Robert A
et al.

Publication Date

2019-03-01

DOI

10.1002/mrm.27501

Peer reviewed

Dynamic Diffusion Weighted Hyperpolarized [13]C Imaging Based on a Slice-Selective Double Spin Echo Sequence for Measurements of Cellular Transport

Xucheng Zhu[1,2], **Jeremy W. Gordon**[1], **Robert A. Bok**[1], **John Kurhanewicz**[1], and **Dr. Peder E.Z. Larson**[1,2,*]

[1.] Department of Radiology and Biomedical Imaging, University of California, San Francisco, San Francisco, CA, United States

[2.] UCSF/UC Berkeley Graduate Program in Bioengineering, University of California, San Francisco, San Francisco, CA, United States

Abstract

Purpose: To develop a pulse sequence to dynamically measure the ADC of hyperpolarized substrates during their perfusion, metabolic conversion, and transport.

Methods: We proposed a slice-selective double spin echo sequence for dynamic hyperpolarized 13C dynamic diffusion weighted imaging. The proposed pulse sequence was optimized for a high field preclinical scanner through theoretical analysis and simulation. The performance of the method was compared to non-slice-selective double spin echo via in vivo studies. We also validated the sequence for dynamic ADC measurement in both phantom studies and transgenic mouse model of prostate cancer studies.

Results: The optimized pulse sequence outperforms the traditional sequence with smaller saturation effects on the magnetization of hyperpolarized compounds which allowed more dynamic imaging frames covering a longer imaging time window. In pre-clinical studies (N = 8), the dynamic hyperpolarized lactate ADC maps of 6 studies in the prostate tumors showed an increase measured ADC over time, which might be related to lactate efflux from the tumor cells.

Conclusions: The proposed sequence was validated and shown to improve dynamic diffusion weighted imaging compared to the traditional double spin echo sequence, providing ADC maps of lactate through time.

Keywords

Hyperpolarized ^{13}C; ADC mapping; dynamic imaging; metabolic imaging

[*]Corresponding author: Peder E.Z. Larson, 1700 4th St, Room 102C, San Francisco, CA 94143, Tel: (415) 415-4876, Fax: (415) 415-4451, peder.larson@ucsf.edu.

Introduction

Characterizing metabolism is key to cancer diagnosis and treatment. As compared to normal tissue, cancer is oftentimes characterized by abnormally high aerobic glycolysis, a phenomenon called the Warburg effect[1]. By using dynamic nuclear polarization (DNP), ^{13}C spins can be polarized to four orders of magnitude greater than the Boltzmann equilibrium polarization level, a process called hyperpolarization[2], which permits imaging the polarized substrates and downstream metabolic products. Hyperpolarized (HP) ^{13}C MRI has shown the potential to non-invasively identifying tumors, such as brain tumors[3,4], and prostate cancer[5,6]. These studies used gradient echo (GRE) based acquisitions to image dynamic changes of the HP ^{13}C spectrum following injection of the HP agent[7–9]. The dynamic images data were fit to a 2–site exchange model to quantify the metabolism by measuring the conversion constant (k_{PL}) between pyruvate to lactate[10–13].

HP ^{13}C also has the potential to measure cellular transport in addition to metabolism, as this dynamic process can have significant contribution during the approximately 1 minute available for imaging. In particular, export of lactate via the monocarboxylate transporters (primarily MCT4) is elevated in many cancers, thus measurements of lactate transport could provide a new biomarker of tumor aggressiveness[14–16].

Thus far, approaches based on frequency shift and diffusion have been applied to measure cellular transport with HP ^{13}C MRI. One study investigated the dynamic distribution of extra- and intracellular HP ^{13}C compounds over time by repeatedly measuring ^{13}C spectrum, which showed a frequency shift between compartments, in cell culture based studies[17]. However, it is challenging to translate this technique for in vivo studies because of the very small (sub-ppm) chemical shift between extra- and intracellular lactate. An alternative way to distinguish the molecules distribution is diffusion-weighted imaging (DWI), which has been well developed for ^1H imaging as a useful tool to identify different microstructures by measuring the apparent diffusion coefficient (ADC) of water[18,19]. In addition, diffusion-weighted ^1H MR spectroscopy can measure ADC of certain metabolites[20,21]. Recently, researchers extended diffusion weighted MRS and MRI to HP ^{13}C studies to measure ADCs of HP ^{13}C metabolites, which provided unique information about the cellular structure and transport of metabolites[22–27]. Unlike proton MRI DWI sequences, HP ^{13}C imaging uses a small tip excitation in each repetition time(TR) and is also more sensitive to refocus pulse imperfections that can saturate HP magnetization[28]. Previous studies developed a double spin echo (DSE), single shot EPI sequence to improve DWI of HP ^{13}C metabolites[29,30]. The DSE sequence was applied to ADC measurement for both solution state[31] and preclinical in vivo studies[30]. In contrast to signal intensity based measurements, such as pyruvate-to-lactate ratio or k_{PL}, HP ADC could provide extra information about microenvironment or microstructure around metabolites[24,26].

However, a single time point ADC measurement depends on not only metabolite distribution, but also the rates of metabolic conversion, injection timing and duration, imaging timing and duration, and thus may not be reliable enough to accurately describe the metabolism and cellular transport processes. We hypothesize that looking at the relative ADC change over time, rather than the ADC value at a single time point, will be more robust

to conversion, perfusion, timing and cellularity differences for improved measurements of lactate efflux. To achieve that goal, some practical problems must be solved. In many experiments, including in pre-clinical scanners, the ^{13}C channel transmit coil is usually smaller than the subject. At the edge of the transmit coil, called the fringe area, B_1^+ is much lower than at the center of the coil. In this region, refocusing pulses can act as a saturation pulses, destroying some of the non-recoverable HP ^{13}C magnetization[32].

In this work, we improved the previous non-slice-selective DSE sequence (ns-DSE) for HP ^{13}C MRI by adding slice-selective gradients to each refocusing pulse (ss-DSE) to minimize saturation effects in the RF coil fringe area. As the ss-DSE inevitably induces saturation effects at the edge of the refocusing area, we optimized the pulse sequence design via simulation to minimize this effect. We compared the performance of DSE sequence with and without slice-selective gradient refocusing pulse through both phantom and in vivo studies. We also investigated the feasibility for dynamic HP metabolites DWI for monitoring cellular transport based on ss-DSE sequence and tested on HP phantom and transgenic adenocarcinoma of the mouse prostate (TRAMP) model.

Methods:

Slice-selective double spin echo sequence design and optimization

The previously used non-slice-selective double spin echo (ns-DSE) sequence consists of a single-band spectral-spatial excitation pulse, two identical hyperbolic secant adiabatic inversion pulse (HS-AFP), and a fly-back echo-planar imaging (EPI) readout[28]. Compared to the ns-DSE sequence, the slice-selective double spin echo (ss-DSE) sequence adds two identical slice-selective gradients on both refocusing pulses to refocus HP ^{13}C spins within the effective area of the transmit coil, in which B_1^+ fulfills the adiabatic condition, shown in Figure 1. The equations related to adiabatic pulse and gradient design are shown:

$$B_1(t) = A\operatorname{sech}\left[\beta\left(t - \frac{T}{2}\right)\right] e^{i\mu\log\left\{\operatorname{sech}\left[\beta\left(t - \frac{T}{2}\right)\right]\right\}} \quad (1)$$

$$BW = \mu\beta/\pi \quad (2)$$

$$A >> \frac{\pi BW}{\gamma\sqrt{\mu}} \quad (3)$$

$$G_z = \frac{2\pi BW}{\gamma \Delta z} \quad (4)$$

In this nomenclature, the RF waveform is in expression (1), where *A* is the peak power of the adiabatic pulse, *β* is the modulation number, *T* is the pulse duration, and μ is the adiabatic factor. The bandwidth(BW)of the pulse is determined by (2), and the peak power of the pulse should fulfill the adiabatic condition determined by Equation (3). Equation (4) determines the gradient strength for the ss-DSE.

For our Varian 14T vertical scanner (Varian, Medical Systems, Inc., Palo Alto, CA), we designed a 10ms duration 9kHz bandwidth pulse with 15 mm slice-selective refocusing thickness, which is well within the homogeneous B1 volume of the coil. At the edge of the selected refocusing slice is the transition area, where the magnetization would be destroyed because the adiabatic condition is not fulfilled. Therefore, the refocusing slice thickness was chosen to be larger than the excitation slice thickness to refocus all the metabolites in every TR, and reduce the transition area effects on imaging slice. The adiabatic factor and RF power were optimized to minimize the transition area through numerical simulation. All the simulations and optimizations were performed based on a modified Bloch equation simulator for HP ^{13}C, which are available online (https://github.com/nicholas-zhu/HP_C13_project.git).

In phantom or in vivo scans, the fringe area effect occurs along the main field direction, therefore, a 1D homogeneous digital phantom was simulated to mimic the real scan setup. To optimize the refocusing pulse and gradient design, the excitation flip angle was set to 0 to look at only the longitudinal magnetization slice profile of the two refocusing pulses for evaluating the ss-DSE performance. The slice profile of the numerical phantom that lost more than 5% magnetization after the ss-DSE was considered as the transition area. Simulations were performed with an adiabatic factor of 5 to 80, bandwidth from 3kHz to 10kHz, and RF power fulfilling adiabatic condition (3). The parameter set with the minimum transition area was selected as the optimized refocusing pulse design.

Hyperpolarization and animal preparation

For HP studies, 24 μL aliquots of HP [1-^{13}C]pyruvate (Cambridge Isotopes, Cambridge, Massachusetts, USA) were polarized for 60 minutes in a HyperSense polarizer (Oxford Instruments) and rapidly dissolved with 4.5 mL NaOH/Tris buffer, yielding 80 mM pyruvate at physiologic pH and temperature.

For in vivo studies, data were acquired in a transgenic mouse model of prostate cancer (TRAMP). Animal studies were performed under a protocol approved by the UCSF Institutional Animal Care and Utilization Committee. Mice were anesthetized with 1–2% isoflurance and maintained at physiological temperature via heating elements. 350 μL HP solution was injected over 15s via tail vein, and the dynamic DSE sequences started at the end of the injection.

Phantom study

After dissolution from the HyperSense, a syringe containing 4mL of HP [1-^{13}C]pyruvate was placed into the coil within the scanner. To reduce the flow effects on ADC mapping of the solution, the imaging sequence started with a 1 minute delay after the syringe was placed

in the scanner. To mimic the in vivo study, the phantoms were scanned in axial plane with 10mm excitation thickness, 15mm refocusing thickness, 2×2 mm^2 in-plane resolution, matrix size 32×32. 10° and 30° flip angles were used alternately to confirm the ADC measurement was not biased by miscalibration of B$_1$ or slice profile effects.

HP ^{13}C Dynamic diffusion imaging

Taking into account the shorter T1 at high field and rapid pyruvate delivery, the acquisition was chosen to start at the end of the ~15 seconds HP [1-^{13}C]pyruvate injection, and the imaging sequence took ~20 seconds. Data were acquired on a 14T vertical scanner with a dual-tuned ^{1}H/^{13}C coil. A high spatial resolution T2–weighted proton image was acquired by using spin echo multi-slice sequence for anatomical reference, TE/TR=20 ms/2000 ms, 20 slices with thickness of 1mm, FOV = 32×32 mm^2, and a matrix size of 192×192. The ^{13}C dynamic DWI acquisition used the ss-DSE sequence, with a single metabolite and single b-value DWI image acquired in each TR. The DSE sequence used a flyback EPI readout, single metabolite 10mm thickness with spectral-spatial excitation, 15mm refocusing thickness with optimized slice-selective refocusing pulse, 2×2 mm^2 in-plane resolution, matrix size 32×32, and time resolution was 3~4 seconds depending on the respiratory gating. After each triggering signal, three b-values (50, 500, 1000 s/mm^2) for a single metabolite were acquired. The excitation flip angle for pyruvate was 10° and lactate was 30°. As we were primarily interested in HP [1-^{13}C]lactate ADC for lactate efflux observation, only one low b-value (50 s/mm^2) pyruvate image was acquired to preserve more magnetization for subsequent lactate imaging.

Data analysis

All the data processing and analysis were implemented in MATLAB (The MathWorks, Inc., Natick, MA). For each excitation, a 16×16 2D k-space data was acquired. For the kidney studies, the imaging FOV was 32×32 mm^2. For TRAMP studies, we used a FOV of 64×64 mm^2 to increase the SNR. The HP ^{13}C images were cropped from 64×64 mm^2 to 32×32 mm^2 to match the FOV of T2 images. For sequence performance comparison, the low b-value images were used for pixel-by-pixel estimations of the overall signal decay rate. T1 decay, magnetization consumption with RF excitation, transition area effects from ss-DSE sequence, and fringe area effects from ns-DSE sequence will all contribute to the overall decay rate.

For dynamic ADC estimation, at each time point, three different b-value DWI images were fit to mono-exponential model pixel-by-pixel with flip angle compensation[30] to calculate the apparent diffusion coefficient (ADC) map. Noise was calibrated with test scan before HP ^{13}C pyruvate injection. Pixels with SNR lower than 5, a ADC fitting R^2 value < 0.95, or a negative ADC value were removed.

Results:

Numerical Simulation

The simulation results of slice-selective refocusing pulse are summarized in Figure 2. According to Figure 2(b), using a higher bandwidth pulse could reduce the transition area

because the slice profile would become sharper, and the spatial shift of the slice between metabolites would get smaller, which would benefit multi-metabolite imaging studies. However, the higher bandwidth pulse requires a higher peak power, shown in Figure 2(c), which would be limited by the RF coils. We set the RF maximum peak power to 2.5G, which matched the maximum B_1^+ of the transmit coil, fixed the time duration to 10ms to reduce TE, and chose the best parameter combination from the transition area map, which was 9kHz for pulse bandwidth and μ=33 (adiabatic factor). The optimized refocusing pulse was used in both phantom and in vivo studies.

In vivo sequence performance comparison

A performance comparison between ss-DSE and ns-DSE in vivo is shown in Figure 3 and Supporting Figure S1. For each study, the experiment was performed twice with the same preparation, one with ss-DSE and the other with ns-DSE but otherwise identical scan parameters. Due to variations in the hyperpolarization level and the exact injected pyruvate dose, the dynamic image intensity was scaled to the first time point image of each scan. According to the dynamic images, signal in the ss-DSE acquisition decayed slower than the signals acquired with ns-DSE. To quantify the comparison, the overall decay rates of pyruvate and lactate were directly calculated without any corrections (e.g. for flip angle or T1 decay compensation). Since the comparison occurred in the same animal, the only different contribution to the signal decay rate should come from acquisition with or without slice-selective gradients. We attribute the more rapid decay rate with the non-slice-selective refocusing pulse to saturation effects arising from fringe area, where the adiabatic condition is not met. The optimized ss-DSE could effectively reduce the saturation effects on HP magnetization compared to ns-DSE sequence to allow for longer dynamic imaging durations. We summarized all comparison experiments, including TRAMP mice tumor imaging (n=3) and healthy mice kidney imaging (n=2), with decay rates in Supporting Table S1. For all the studies, both HP [1-^{13}C]lactate and [1-^{13}C]pyruvate decay rates with ss-DSE acquisition were lower than with ns-DSE, providing higher relative SNR at later time points. In one study, we also evaluated the ss-DSE with an earlier acquisition strategy, starting the acquisition at ~6 seconds after the start of injection, so more pyruvate should flow through the fringe area during the acquisition. According to Figure S1, the ss-DSE had 2~3 times higher signals in later time points compared to ns-DSE.

Dynamic HP ^{13}C DWI

Dynamic DWI phantom results from HP [1-^{13}C]pyruvate are summarized in Supporting Figure S2. The ADC values of the phantom remained stable through time at ~1.4×10^{-3} mm^2/s. We acquired both 10° and 30° DWI images to mimic the in vivo study for pyruvate and lactate. The measured ADC of the phantom was constant through time, indicating that proposed method did not have bias from slice profile effects or incorrect B1 calibration, and that the measurement is independent of dynamic acquisition ordering[30,33], while the slight ADC map inhomogeneity inside the phantom could be caused by flow effects in the solution.

In vivo dynamic DWI studies in TRAMP mice prostate tumors show ADC values that are in good agreement with previous in vivo and ex vivo studies[17,30], and are shown in Figure 4.

The dynamic ADC maps, ADC histograms and average ADC values showed a shift from low to high ADC in the prostate tumor. According to Figure 4 (a), (b), the mean ADCs through time shift from an average $\sim 0.2 \times 10^{-3}$ mm^2/s at the end of injection to $\sim 0.6 \times 10^{-3}$ mm^2/s 12 seconds after the end of injection for this late stage TRAMP mouse. Eight TRAMP mice were imaged with the proposed sequence for dynamic HP [1-^{13}C]lactate ADC measurement, the change of ADCs mean and standard deviation in TRAMP mice (N = 8) prostate tumors are plotted in Figure 5. 6 out of 8 studies showed the increase of mean measured ADC through time. The shift of ADC values is consistent with lactate efflux during the experiment, and the maximum ADC values through time are also consistent with the previous single time point ADC measurements in TRAMP mice[34]. Initially, the ADC values are similar to cell studies that measured an intracellular lactate ADC of around 0.2×10^{-3} mm^2/s[26]. Furthermore, these cell studies measured extracellular lactate ADCs of around 0.6×10^{-3} mm^2/s which is similar to the largest ADC values measured in our studies.

Discussion:

In this work, we designed and optimized a ss-DSE sequence for high field preclinical hyperpolarized ^{13}C dynamic imaging studies. Compared to the traditional ns-DSE sequence, ss-DSE avoids the fringe area effect, which would destroy the magnetization located at the edge of the transmit coil. The ss-DSE was tested via HP [1-^{13}C]pyruvate phantom study, and the benefits of ss-DSE for dynamic imaging were assessed via in vivo studies, including HP dynamic DWI to monitor the lactate microenvironment.

In vivo study comparisons showed that dynamic HP pyruvate signal decayed faster with the ns-DSE sequence than with ss-DSE. As the HP [1-^{13}C]pyruvate was injected through the tail vein, the magnetization of circulating HP [1-^{13}C]pyruvate distributed at the fringe area would be saturated by the refocusing pulse, which would lead to the faster decay of the total HP pyruvate signal. Because HP [1-^{13}C]lactate is primarily converted from intracellular HP [1-^{13}C]pyruvate, the HP lactate signal would largely depend on the influx of HP [1-^{13}C]pyruvate signal. To preserve enough magnetization for dynamic imaging, the imaging timing should be very carefully chosen. Prior studies[35] have developed bolus tracking techniques to monitor the pyruvate signal in the tumor, with the imaging sequence triggered when the HP pyruvate has arrived at the tumor. However, it is inevitable to destroy some magnetization of the circulating pyruvate if we want to start imaging as soon as the pyruvate arrives in the target region. In contrast, the ss-DSE sequence is largely unaffected by the pyruvate spatial distribution, delivery and imaging timing, which would make spin-echoes imaging and T2 sampling more feasible for clinical HP studies.

We also validated the feasibility of ss-DSE based dynamic HP ^{13}C DWI in TRAMP mouse studies. Several effects would contribute to ADC variations in tumor imaging. The cellularity of prostate tumors has a negative correlation with ^{1}H ADC changes, with late stage tumors having higher cellularity and a lower ^{1}H ADC compared to early stage[36]. However, the extra- and intracellular molecular distribution of the HP metabolites will also determine the ^{13}C ADC values, with late-stage TRAMP tumors having higher glycolysis that is usually associated with the more lactate efflux and thus a higher expected lactate ADC[24]. Considering the combination of tumor cellularity and lactate efflux, it has been

difficult for us to distinguish tumor stage with the single measured ADC value. The dynamic ADC measurements indirectly reflect the change of the extra- versus intracellular molecular distribution, which might help to distinguish the effects of cellularity from lactate efflux. The lactate ADC increasing over time might indicate a rapid lactate efflux, while the ADC remaining constant or decreasing might reflect slower lactate efflux. These relationships among lactate efflux, dynamic HP images, and dynamic HP ADC change must be validated in future studies.

The ss-DSE approach will be also valuable for clinical scans. In clinical scanners, current 13C transmit coils have limited spatial coverage and do not cover the entire body, so non-selective spin echo based methods will inevitably have large fringe area effects. Even dedicated ^{13}C body coils will likely not cover the entire body. Thus in clinical scans, the ss-DSE sequence could limit the transition area to preserve more magnetization for dynamic imaging.

However, this work still has room to improve. Firstly, HP ^{13}C pyruvate and lactate have shorter T1 at 14T than 3T, so to cover a longer time range ADC measurement the proposed methods should be implemented and tested on 3T. At 3T, the main change of the acquisition would be the spectral-spatial excitation design, which should have a longer duration to excite the same spectral profile as on a 14T scanner. For systems without high performance gradients, the diffusion gradients must also be increased in duration to attain the desired b-value, and large slew rates might cause peripheral nerve stimulation. These will both contribute to a longer TE (around 180ms) and longer diffusion time to achieve the same b-values as the preclinical scanner[30], increasing sensitivity to bulk motion and reducing SNR due to T2 decay. Secondly, to maximize the scan SNR efficiency and increase the effective dynamic imaging time points, a variable flip angle(VFA) scheme could help[37,38]. In this work, we kept the flip angle constant through the scan to simplify the data analysis. When multiple b-value images are acquired, VFA could be also optimized for different b-value to ensure enough SNR images for ADC estimation. However, VFA schemes are more susceptible to B1 errors, so B1 field measurements would be crucial for an accurate VFA approach. In addition, changing the b-value ordering to acquire high b-value DWI images first would increase the SNR of high b-value images, which might improve the ADC estimation as well. Thirdly, in molecular compartmentalization assessment studies, a multi-exponential fitting model is most appropriate. However, in this study, we simplified the model to a mono-exponential fit due to only having acquired 3 b-value images.

Conclusions:

In this work, we proposed a slice-selective double spin echo sequence for dynamic HP ^{13}C imaging. Performance of the proposed optimized sequence was compared to the previous non-slice-selective double spin echo sequence through in vivo studies. And, for the first time, we investigated measuring dynamic ADC maps of HP ^{13}C metabolites by using the proposed sequence. Our initial studies in TRAMP mice prostate tumors showed an increase in lactate ADC over time, consistent with increased MCT4 expression and lactate efflux in late-stage TRAMP prostate tumors. These dynamic ADC changes have the potential to improve the assessment of aggressive cancers by providing a measure of lactate efflux.

Supplementary Material

Refer to Web version on PubMed Central for supplementary material.

Acknowledgement:

Reference:

1. Pavlides S, Whitaker-Menezes D, Castello-Cros R, et al. The reverse Warburg effect: Aerobic glycolysis in cancer associated fibroblasts and the tumor stroma. Cell Cycle. 2009;8(23):3984–4001. doi:10.4161/cc.8.23.10238. [PubMed: 19923890]

2. Ardenkjaer-Larsen JH, Fridlund B, Gram A, et al. Increase in signal-to-noise ratio of > 10,000 times in liquid-state NMR. Proc Natl Acad Sci. 2003;100(18):10158–10163. doi:10.1073/pnas.1733835100. [PubMed: 12930897]

3. Albers MJ, Bok R, Chen AP, et al. Hyperpolarized 13C lactate, pyruvate, and alanine: Noninvasive biomarkers for prostate cancer detection and grading. Cancer Res. 2008;68(20):8607–8615. doi:10.1158/0008-5472.CAN-08-0749. [PubMed: 18922937]

4. Golman K, Zandt R i., Lerche M, Pehrson R, Ardenkjaer-Larsen JH. Metabolic Imaging by Hyperpolarized 13C Magnetic Resonance Imaging for In vivo Tumor Diagnosis. Cancer Res. 2006;66(22):10855–10860. doi:10.1158/0008-5472.CAN-06-2564. [PubMed: 17108122]

5. Keshari KR, Sriram R, Van Criekinge M, et al. Metabolic Reprogramming and Validation of Hyperpolarized ^{13}C Lactate as a Prostate Cancer Biomarker Using a Human Prostate Tissue Slice Culture Bioreactor. Prostate. 2013;73(11):1171–1181. doi:10.1002/pros.22665. [PubMed: 23532911]

6. Nelson SJ, Kurhanewicz J, Vigneron DB, et al. Metabolic Imaging of Patients with Prostate Cancer Using Hyperpolarized[1–13C] Pyruvate. Sci Transl Med. 2013;5(198):198ra108. doi:10.1126/scitranslmed.3006070.

7. Mayer D, Yen YF, Tropp J, Pfefferbaum A, Hurd RE, Spielman DM. Application of subsecond spiral chemical shift imaging to real-time multislice metabolic imaging of the rat in vivo after injection of hyperpolarized 13C1–pyruvate. Magn Reson Med. 2009;62(3):557–564. doi:10.1002/mrm.22041. [PubMed: 19585607]

8. Kohler SJ, Yen Y, Wolber J, et al. In vivo 13carbon metabolic imaging at 3T with hyperpolarized 13C–1-pyruvate. Magn Reson Med. 2007;58(1):65–69. doi:10.1002/mrm.21253. [PubMed: 17659629]

9. Golman K, in 't Zandt R, Thaning M. Real-time metabolic imaging. Proc Natl Acad Sci. 2006;103(30):11270–11275. doi:10.1073/pnas.0601319103. [PubMed: 16837573]

10. Von Morze C, Larson PEZ, Hu S, et al. Investigating tumor perfusion and metabolism using multiple hyperpolarized13C compounds: HP001, pyruvate and urea. Magn Reson Imaging. 2012;30(3):305–311. doi:10.1016/j.mri.2011.09.026. [PubMed: 22169407]

11. Kettunen MI, Hu DE, Witney TH, et al. Magnetization transfer Measurements of exchange between hyperpolarized [1–13C]pyruvate and [1–13C]lactate in a murine lymphoma. Magn Reson Med. 2010;63(4):872–880. doi:10.1002/mrm.22276. [PubMed: 20373388]

12. Harris T, Eliyahu G, Frydman L, Degani H. Kinetics of hyperpolarized 13C1–pyruvate transport and metabolism in living human breast cancer cells. Proc Natl Acad Sci U S A. 2009;106(43):18131–18136. doi:10.1073/pnas.0909049106. [PubMed: 19826085]

13. Harrison C, Yang C, Jindal A, et al. Comparison of kinetic models for analysis of pyruvate-to-lactate exchange by hyperpolarized 13C NMR. NMR Biomed. 2012;25(11):1286–1294. doi:10.1002/nbm.2801. [PubMed: 22451442]

14. Floch L, Chiche J, Marchiq I, et al. CD147 subunit of lactate/H+ symporters MCT1 and hypoxia-inducible MCT4 is critical for energetics and growth of glycolytic tumors. Proc Natl Acad Sci. 2012;109(49):20166–20166. doi:10.1073/pnas.1219161109.

15. Dimmer KS, Friedrich B, Lang F, Deitmer JW, Bröer S. The low-affinity monocarboxylate transporter MCT4 is adapted to the export of lactate in highly glycolytic cells. Biochem J 2000;350Pt1(1):219–227. doi:10.1042/0264-6021:3500219.

16. Pinheiro C, Longatto-Filho A, Azevedo-Silva J, Casal M, Schmitt FC, Baltazar F. Role of monocarboxylate transporters in human cancers: State of the art. J Bioenerg Biomembr. 2012;44(1):127–139. doi:10.1007/s10863-012-9428-1. [PubMed: 22407107]

17. Sriram R, Van Criekinge M, Hansen A, et al. Real-time measurement of hyperpolarized lactate production and efflux as a biomarker of tumor aggressiveness in an MR compatible 3D cell culture bioreactor. NMR Biomed. 2015;28(9):1141–1149. doi:10.1002/nbm.3354. [PubMed: 26202449]

18. Kono K, Inoue Y, Nakayama K, et al. The role of diffusion-weighted imaging in patients with brain tumors. AJNR Am J Neuroradiol. 2001;22(6):1081–1088. papers3://publication/uuid/C2BFF7E3–8CD1–4EA6–8958-0484D3DC298F. [PubMed: 11415902]

19. Haider MA, Van Der Kwast TH, Tanguay J, et al. Combined T2–weighted and diffusion-weighted MRI for localization of prostate cancer. Am J Roentgenol. 2007;189(2):323–328. doi:10.2214/AJR.07.2211. [PubMed: 17646457]

20. Hakumaki JM, Poptani H, Puumalainen AM, et al. Quantitative H–1 nuclear magnetic resonance diffusion spectroscopy of BT4C rat glioma during thymidine kinase- mediated gene therapy in vivo: Identification of apoptotic response. Cancer Res. 1998;58(17):3791–3799. [PubMed: 9731486]

21. Harada M, Uno M, Hong F, Hisaoka S, Nishitani H, Matsuda T. Diffusion-weighted in vivo localized proton MR spectroscopy of human cerebral ischemia and tumor. NMR Biomed. 2002;15(1):69–74. doi:10.1002/nbm.759. [PubMed: 11840555]

22. Schilling F, Düwel S, Köllisch U, et al. Diffusion of hyperpolarized 13C-metabolites in tumor cell spheroids using real-time NMR spectroscopy. NMR Biomed. 2013;26(5):557–568. doi:10.1002/nbm.2892. [PubMed: 23233311]

23. Vejby L, Schilling F, Janich MA, Menzel MI, Ardenkjær-larsen JH. In vivo measurement of apparent diffusion coefficients of hyperpolarized 13 C-labeled metabolites. 2014;(1). doi:10.1002/nbm.3093.

24. Feuerecker B, Durst M, Michalik M, et al. Hyperpolarized 13C Diffusion MRS of Co-Polarized Pyruvate and Fumarate to Measure Lactate Export and Necrosis. J Cancer. 2017;8(15):3078–3085. doi:10.7150/jca.20250. [PubMed: 28928899]

25. Patrick PS, Kettunen MI, Tee S-S, et al. Detection of transgene expression using hyperpolarized 13 C urea and diffusion-weighted magnetic resonance spectroscopy. Magn Reson Med. 2015;73(4):1401–1406. doi:10.1002/mrm.25254. [PubMed: 24733406]

26. Koelsch BL, Sriram R, Keshari KR, et al. Separation of extra- and intracellular metabolites using hyperpolarized13C diffusion weighted MR. J Magn Reson. 2016;270:115–123. doi:10.1016/j.jmr.2016.07.002. [PubMed: 27434780]

27. Kettunen MI, Kennedy BWC, Hu DE, Brindle KM. Spin echo measurements of the extravasation and tumor cell uptake of hyperpolarized [1–13C]lactate and [1–13C]pyruvate. Magn Reson Med. 2013;70(5):1200–1209. doi:10.1002/mrm.24591. [PubMed: 23280500]

28. Cunningham CH, Chen AP, Albers MJ, et al. Double spin-echo sequence for rapid spectroscopic imaging of hyperpolarized 13C. J Magn Reson. 2007;187(2):357–362. doi:10.1016/j.jmr.2007.05.014. [PubMed: 17562376]

29. Reese TG, Heid O, Weisskoff RM, Wedeen VJ. Reduction of eddy-current-induced distortion in diffusion MRI using a twice-refocused spin echo. Magn Reson Med. 2003;49(1):177–182. doi:10.1002/mrm.10308. [PubMed: 12509835]

30. Koelsch BL, Reed GD, Keshari KR, et al. Rapid in vivo apparent diffusion coefficient mapping of hyperpolarized ^{13}C metabolites. Magn Reson Med 2015;74(3):622–633. doi:10.1002/mrm.25422. [PubMed: 25213126]

31. Koelsch BL, Keshari KR, Peeters TH, Larson PEZ, Wilson DM, Kurhanewicz J. Diffusion MR of hyperpolarized 13C molecules in solution. Analyst. 2013;138(4):1011. doi:10.1039/c2an36715g. [PubMed: 23304699]

32. Josan S, Yen YF, Hurd R, Pfefferbaum A, Spielman D, Mayer D. Application of double spin echo spiral chemical shift imaging to rapid metabolic mapping of hyperpolarized [1 –13C]-pyruvate. J Magn Reson. 2011;209(2):332–336. doi:10.1016/j.jmr.2011.01.010. [PubMed: 21316280]

33. Gordon JW, Milshteyn E, Marco-Rius I, Ohliger M, Vigneron DB, Larson PEZ. Mis-estimation and bias of hyperpolarized apparent diffusion coefficient measurements due to slice profile effects. Magn Reson Med 2017;78(3):1087–1092. doi:10.1002/mrm.26482. [PubMed: 27735082]

34. Gordon JW, Qin H, Sriram R, et al. In Vivo Hyperpolarized 13C Diffusion Weighted MRI Measures Lactate Efflux and Changes in MCT4 Expression in Prostate Cancer In: In Proceedings of the 24th Annual Meeting of ISMRM, 2016 p. 3676.

35. Durst M, Koellisch U, Gringeri C, et al. Bolus tracking for improved metabolic imaging of hyperpolarised compounds. J Magn Reson. 2014;243:40–46. doi:10.1016/j.jmr.2014.02.011. [PubMed: 24717443]

36. Ellingson BM, Malkin MG, Rand SD, et al. Validation of functional diffusion maps (fDMs) as a biomarker for human glioma cellularity. J Magn Reson Imaging. 2010;31(3):538–548. doi: 10.1002/jmri.22068. [PubMed: 20187195]

37. Maidens J, Gordon JW, Arcak M, Larson PEZ. Optimizing Flip Angles for Metabolic Rate Estimation in Hyperpolarized. IEEE Trans Med Imaging. 2016;35(11):2403–2412. [PubMed: 27249825]

38. Larson PEZ, Bok R, Kerr AB, et al. Investigation of tumor hyperpolarized [1–13C]-pyruvate dynamics using time-resolved multiband RF excitation echo-planar MRSI. Magn Reson Med. 2010;63(3):582–591. doi:10.1002/mrm.22264. [PubMed: 20187172]
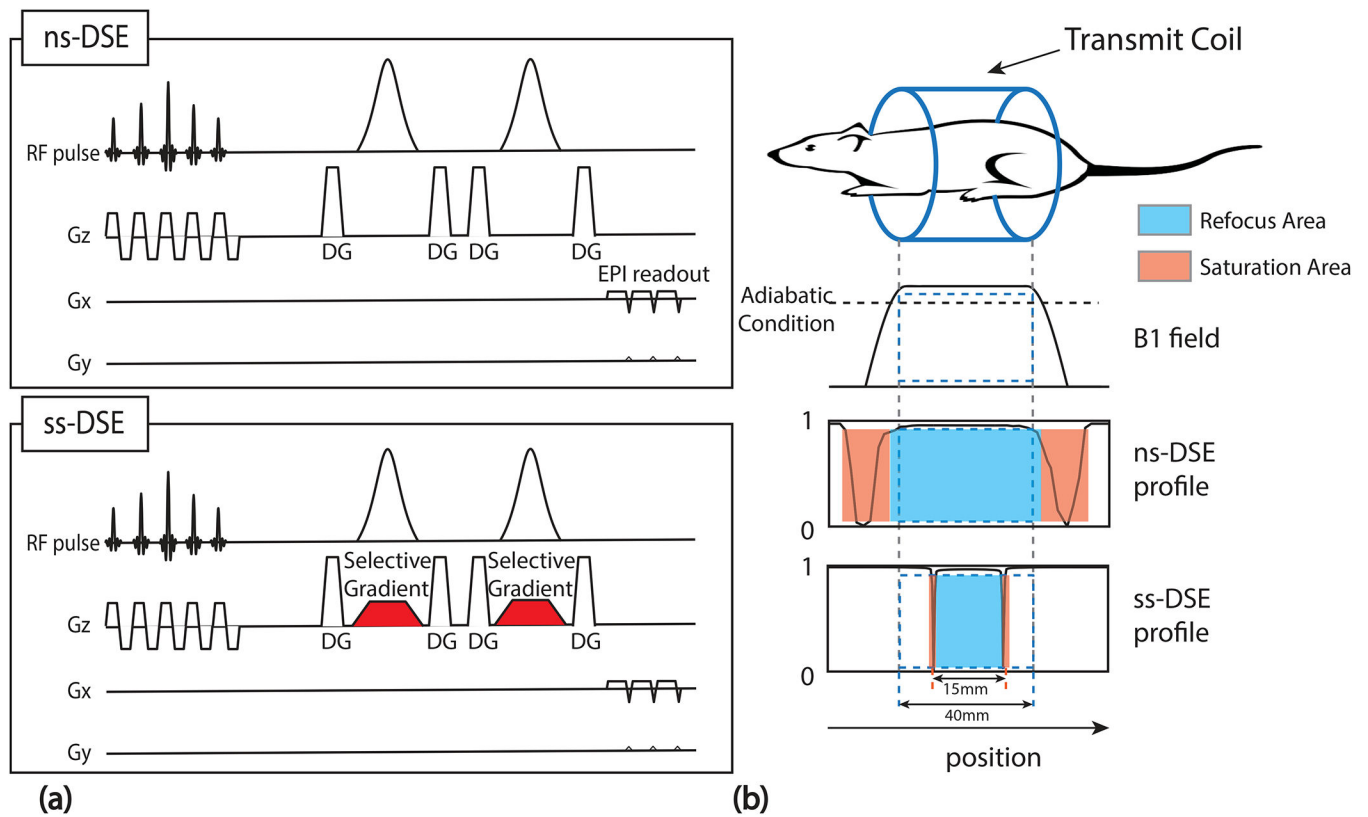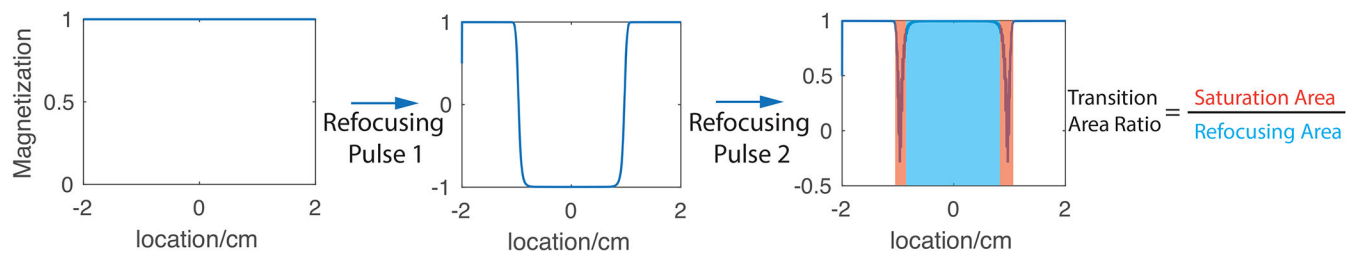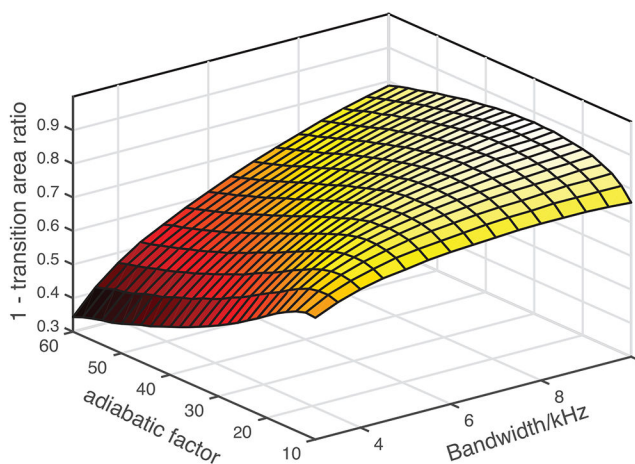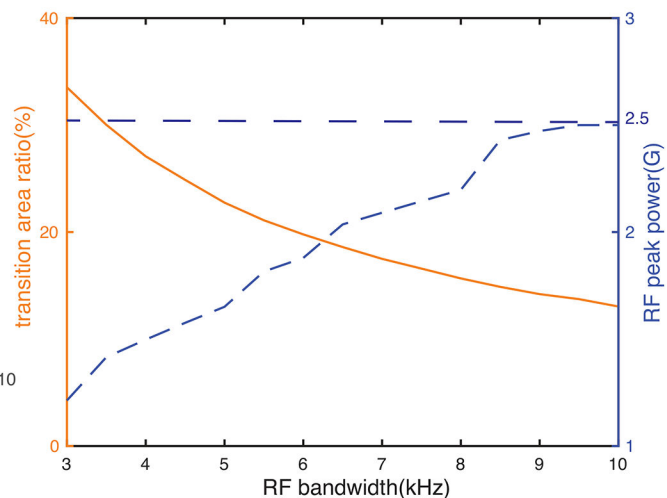
Figure 1.
Comparison of ss-DSE (slice-selective) and ns-DSE (non-selective) methods. The ss-DSE adds two identical slice selective gradients on the refocusing pulses, as illustrated in (a), to refocus a smaller area. In many experiments, the transmit coil is smaller than the scan object, so at the edge of the coil the B1+ could not fulfill the adiabatic condition for the refocusing pulses. Compared to ns-DSE profile that includes these fringe effects, the ss-DSE profile can have a much smaller saturation area by using a high bandwidth refocusing pulse, as illustrated in (b).

Figure 2.
Refocusing pulse optimization. Refocusing performance was evaluated through numerical simulation, and an optimized parameters combination was selected based on the transition area ratio (a). The transition area ratio of the optimized parameter combinations decreases as the RF bandwidth increases; however, the required RF peak power also increases, as shown in (b). The maximum RF power was limited to 2.5G, and the pulse parameters of BW=9kHz, μ=33 were chosen for all studies, shown in (c).
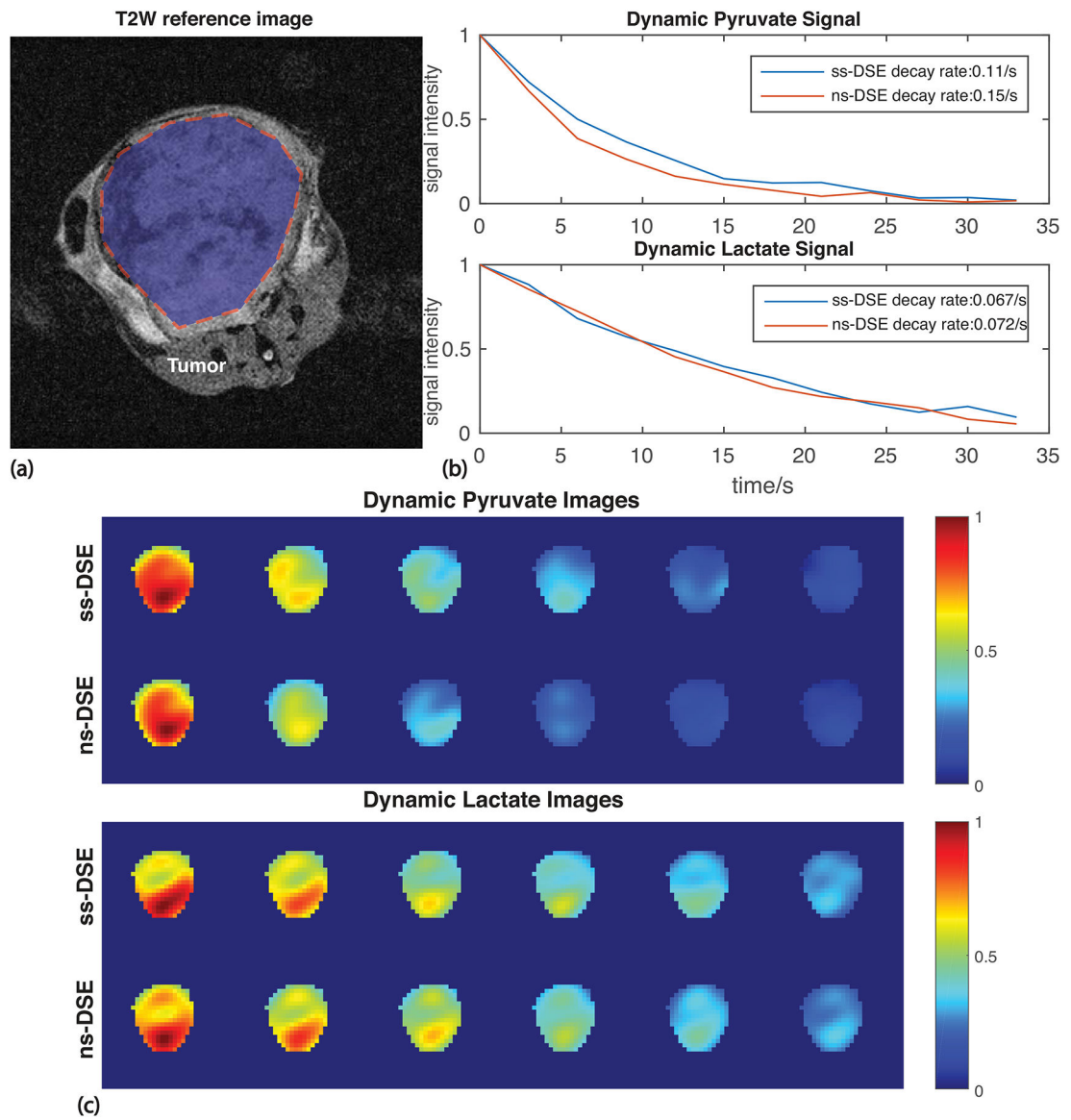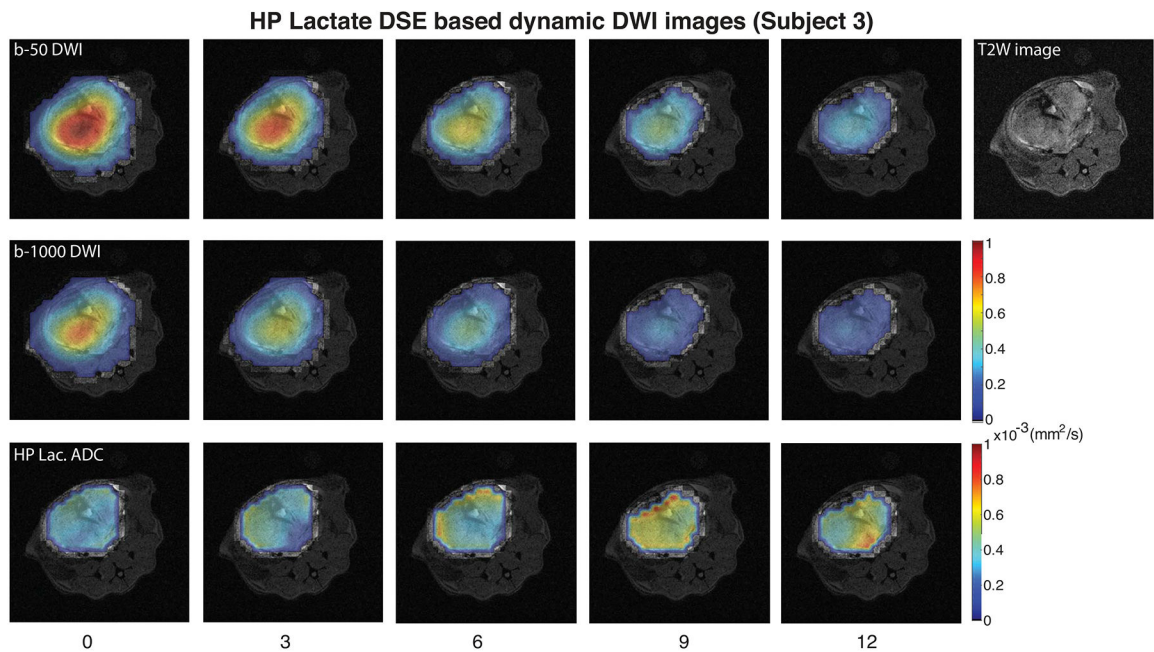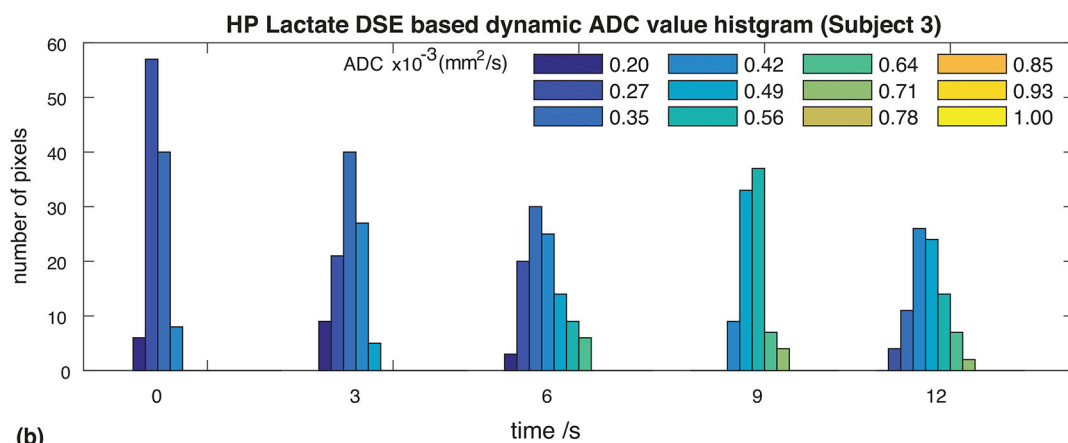
Figure 3.
ss-DSE (slice-selective) and ns-DSE (non-selective) dynamic image comparison. The anatomical T2 weighted image is shown in (a). The total signals and the dynamic images of the ROI (tumor) at different time points are plotted in (b), and (c). The apparent signal decay rate of the HP pyruvate acquired with ss-DSE was much slower than with ns-DSE.

Figure 4.
In vivo dynamic ADC measurement. The HP 13C images are cropped to the same FOV with the 1H images. Dynamic HP lactate low b-value (50 mm2/s), high b-value (1000 mm2/s) DWI images, and ADC maps over anatomical images are shown in (a), for the display purposes, we linearly interpolated ADC maps to the resolution of T2 image. The histograms of ADC values at each time point are shown in (b). The ADCs distribution shifts from low ADC values immediately following the injections, with increasing to high ADC values over time, indicated a change in the HP lactate microenvironment.
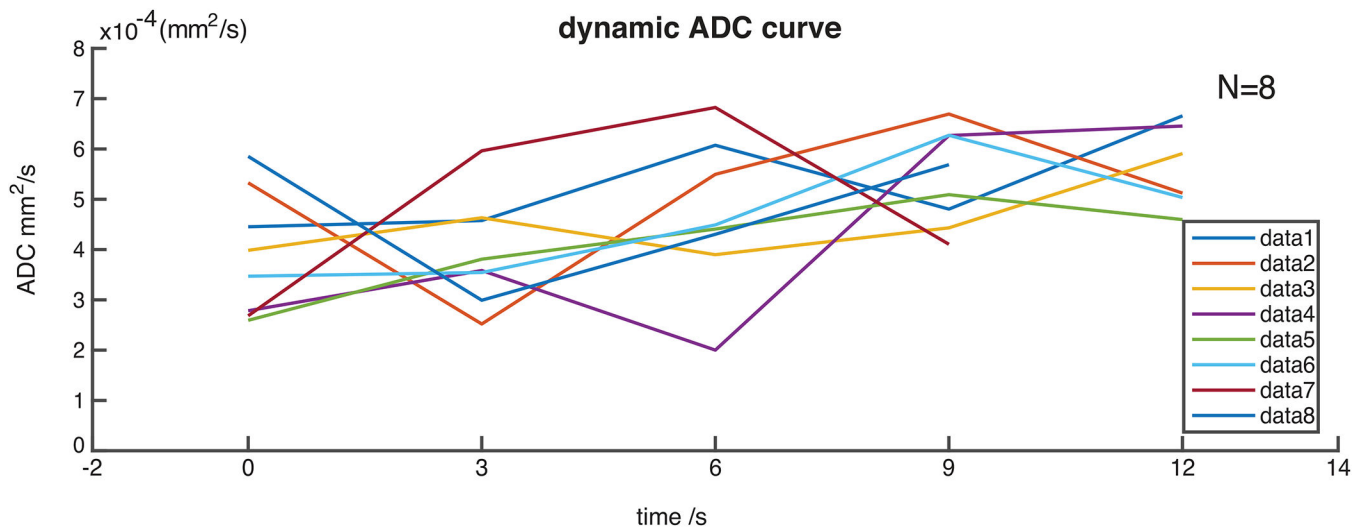
Figure 5.
Dynamic ADC measurement on different subjects. Dynamic mean ADC values of different TRAMP subjects (N = 8) are plotted. 2 of 8 the studies (Data 1 and 7) only have 4 dynamic time points data due to not enough SNR for ADC measurement at the last time points. 6 out of 8 studies showed the increase of mean measured ADCs through time.